SANDIA REPORT

SAND2014-17645
Unlimited Release
Printed September 2014

Characterization of Tri-lab Tantalum (Ta) Plate

Thomas E. Buchheit, Ellen K. Cerreta, Lisa Diebler, Shuh-Rong Chen, Joseph R. Michael

Prepared by
Sandia National Laboratories
Albuquerque, New Mexico 87185 and Livermore, California 94550

Sandia National Laboratories is a multi-program laboratory managed and operated by Sandia Corporation, a wholly owned subsidiary of Lockheed Martin Corporation, for the U.S. Department of Energy's National Nuclear Security Administration under contract DE-AC04-94AL85000.

Issued by Sandia National Laboratories, operated for the United States Department of Energy by Sandia Corporation.

Available to DOE and DOE contractors from
U.S. Department of Energy
Office of Scientific and Technical Information
P.O. Box 62
Oak Ridge, TN 37831

Telephone: (865) 576-8401
Facsimile: (865) 576-5728
E-Mail: reports@adonis.osti.gov
Online ordering: http://www.osti.gov/bridge

Available to the public from
U.S. Department of Commerce
National Technical Information Service
5285 Port Royal Rd.
Springfield, VA 22161

Telephone: (800) 553-6847
Facsimile: (703) 605-6900
E-Mail: orders@ntis.fedworld.gov
Online order: http://www.ntis.gov/help/ordermethods.asp?loc=7-4-0#online

SAND2014-17645
Unlimited Release
Printed Month Year

Characterization of Tri-lab Tantalum (Ta) plate

Thomas E. Buchheit, Ellen Cerreta, Lisa Deibler, Shuh-Rong Chen, Joseph R. Micheal
Materials and Process Science Center
Sandia National Laboratories
P.O. Box 5800
Albuquerque, New Mexico 87185

Materials Science and Technology Division, MST-8
Los Alamos National Laboratory
Mail Stop G755
Los Alamos, New Mexico 87545

Abstract

This report provides a detailed characterization Tri-lab Tantalum (Ta) plate jointly purchased from HCStark Inc. by Sandia, Los Alamos and Lawrence Livermore National Laboratories. Data in this report was compiled from series of material and properties characterization experiments carried out at Sandia (SNL) and Los Alamos (LANL) Laboratories through a leveraged effort funded by the C2 campaign. Results include microstructure characterization detailing the crystallographic texture of the material and an increase in grain size near the end of the rolled plate. Mechanical properties evaluations include, compression cylinder, sub-scale tension specimen, micohardness and instrumented indentation testing. The plate was found to have vastly superior uniformity when compare with previously characterized wrought Ta material. Small but measurable variations in microstructure and properties were noted at the end, and at the top and bottom edges of the plate.

ACKNOWLEDGMENTS

LANL authors wish to thank the support and technical contributions from J.F. Bingert, G.T. Gray III, C.P. Trujillo, and M.F. Lopez. The authors also gratefully acknowledge Tyler Payton for assistance with mechanical testing at SNL.

CONTENTS

FIGURES

Figure 3.9- Comparison of Tension and Compression Stress-Strain curves.

Figure 3.10 –Grids of microhardness measurements extending from the edge toward the middle of a cross-sectioned sample taken from the center and the end of the Ta-plate.

Figure 3.11 Instrumented indentation results on Ta plate cross-sections.

TABLES

NOMENCLATURE

DOE	Department of Energy
SNL	Sandia National Laboratories
LANL	Los Alamos National Laboratories
LLNL	Lawrence Livermore National Laboratories
Ta	Tantalum
BCC	Body Centered Cubic crystal structure
PF	Pole Figure
IPF	Inverse Pole Figure
RD	Rolling Direction
ND	Normal Direction
TD	Transverse Direction
GPa	GigaPascals
TT	Through thickness
IP	In-plane
IPA	In-plane co-aligned with last pass rolling direction
IPB	In-plane co-aligned perpendiculat to last pass rolling direction

1. INTRODUCTION

A large single batch of Tantalum (Ta) plate material produced by HC Stark Inc. (www.hcstark.com) was jointly purchased by Sandia (SNL), Livermore (LLNL), and Los Alamos (LANL) National Laboratories permitting the individual DOE labs to perform investigations on the same processed material. For this to be the case, Ta material obtained had to be microstructurally similar from plate to plate, thus ensuring that properties would also be similar. Another important goal of the joint purchase was to have material that was homogenous within a plate. With baseline material optimized for microstructure and properties uniformity, experiments performed across the labs could be compared directly and/or utilized together to build a common database for the understanding of this class of materials' performance. Specifically, a thread of similarity would exist between experiments conducted at the high rate test facilities at LANL, National Ignition Facility (NIF) at LLNL and Z-pinch at SNL. Through a single large procurement, the Ta plate material was distributed amongst the laboratories. Initial characterization of the material microstructure and its properties has been performed to determine the extent to which desired material characteristics, uniformity and homogeneity, match with actual material characteristics.

In this Joint Report prepared by SNL and LANL, the initial material characterization, which includes details of microstructure and properties of the Ta plate material, henceforth designated as the *tri-lab Ta plate*, is provided.

Goal: Establish the extent to which there exists uniform microstructure and crystallographic texture throughout a single Ta plate. The relationship of this microstructure to mechanical properties is also established. Finally, a direct comparison of select microstructural features and properties is carried out.

1.1 Material

The original Tri-Lab Ta plate material specifications, chemistry and processing, as provided by the manufacturer, are provided here.

Specifications:
Disk shape: Typical Plate size- 0.4" (10.16 mm) thick by 17.5" (44.5 mm) dia. A total of 9 plates were purchased, Each Lab was given 3 plates. One such plate is shown in Figure 1.1.

Chemistry:
The chemistry conforms to specification provided by ASTM B-708-05. Most significant measured impurities are O (16 PPM), N (8 PPM), C (5 PPM) and H (1 PPM).

Processing:
Processing a metal or metal alloy from an as-cast or as-cast and homogenized condition to a finished form such as the rolled plate illustrated in Figure 1.1 requires several steps. Plate rolling, as a directional deformation process, commonly leads to microstructural characteristics of banding and preferred crystallographic orientations typically referred to as crystallographic texture. These microstructural variations can lead to a directional dependence and local variations in mechanical properties. Furthermore, a portion of a multi-step, plate-rolling process

that also contributes to microstructure and property variation in the finished plate includes heat treatments, either during rolling (hot rolling) or through successive deformation+anneal cycles. Heat treatment affects microstructure through grain growth and the process of microstructural recrystallization. In turn, grain growth can be non-uniform in the plate and the recrystallization process can lead to abnormal grain growth further driving local properties variations in processed BCC metals [1].

In general, banding and crystallographic texture in processed polycrystalline BCC (body-centered cubic) metals, such as tantalum, is notoriously difficult to control. [2] [3] [4] In spite of this, the tri-lab Ta plate provided by HCStark exhibited a degree of uniformity far superior to similar material, historically characterized by LANL, as will be presented in the succeeding sections. The uniformity was achieved, in part, by specialized rolling methods: clock rolling and asymmetric tilt rolling of Ta stock material. [5] [6, 7] However, perfect homogeneity in a cast and processed polycrystalline material, especially a BCC metal whose characteristics seem to inherently resist homogeneity, is nearly impossible. Thus, this report documents characteristics of the tri-lab plate material, primarily measured across two separate plates, one residing at LANL (E2789-4-4-10553-19212) and the other at SNL (E2789-2-3-10553-19206) focusing on any directional or local inhomogeneity in the plate which may impact future experiments on the plate material. The plates will simply be referred to as #19212 and #19206 and a distinguishing feature of the plates is that they originated from different billets of material.

1.2 Structure of the Report

The results contained within this report are presented in two sections: section 3 reviewing the microstructure characterization and section 4 reviewing the mechanical properties characterization. Since microstructural characterization focuses on crystallographic texture and local variations in crystallographic texture obtained by EBSD imaging, a brief review of the relevant aspects of crystallographic texture is given in section 2.

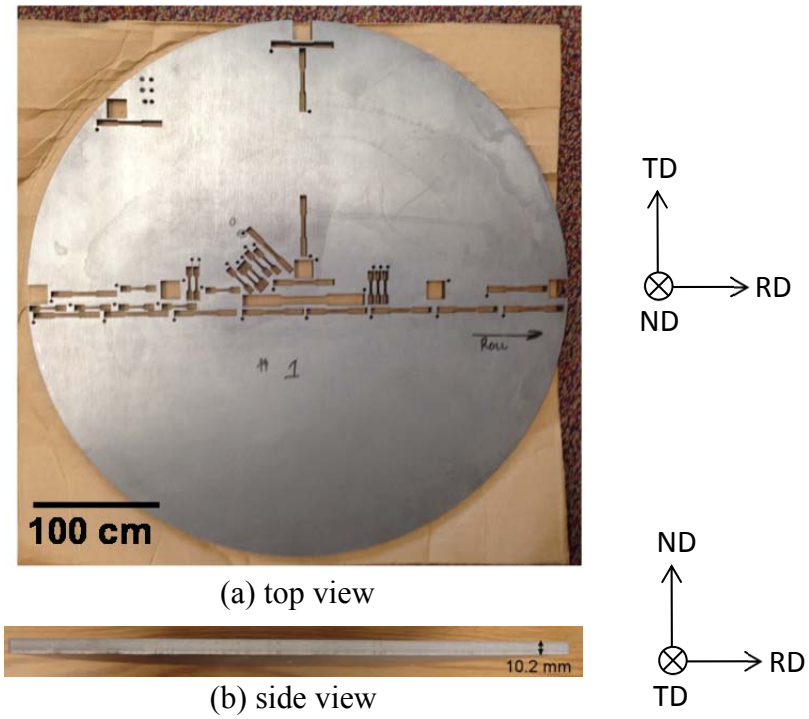

(a) top view

(b) side view

Figure 1.1- Photographs of HC Stark Tri-lab Ta plate (#19206).

1.3 Microstructure and Crystallographic Texture in BCC Metals

Processed BCC metals and alloys tend to form crystallographic fiber textures, where grains within the material preferentially align with one globally defined processing direction [3] [4] [8]. In pure tantalum, cold rolling produces a relatively strong α-fiber texture, defined by grains with their ⟨110⟩ crystallographic directions aligned with the plate rolling direction. Also commonly found in BCC metal rolling textures is a weaker but present γ-fiber texture, defined by grain orientations with their ⟨111⟩ directions aligned with the plate normal direction.

Crystallographic texture in this report is presented using inverse pole figures (IPFs) and stereographic projection plots, also referred to as pole figures (PFs). Often texture is reported along principle directions defined by a crystal unit cell. For a BCC metal, the three principal directions [001], [101], and [111] defined within a standard unit cell, depicted in Figure 1.2, define a unit triangle. The triangle, distinguished by the dashed lines, can be projected on to a sphere and planarized into a stereographic or equal area form such as those depicted in Figure 1.3 and 1.4. Additional mathematical details of the projection method are given in several textbook references [9]. Due to symmetry in a BCC crystal, any triangle bounded by a ⟨001⟩-type, ⟨101⟩-type or ⟨111⟩-type direction (square brackets define a specific direction, angled brackets define a family of directions per standard Miller indices notation) leads to a *symmetrically indistinguishable unit triangle*. The triangle depicted in Figure 1.2 is the commonly chosen one for the IPF representation. An IPF depicts a globally defined direction in crystallographic coordinates. In terms of a rolled plate of material, the globally defined directions are shown in Figure 1.1. They are **RD**, *the plate rolling direction* (in this report, the last pass rolling direction), **TD** *the transverse direction* and **ND** *the normal to the plane of rolling*. Together, the three directions define an orthogonal coordinate system and any one of the directions can be plotted in the crystallographically defined coordinate system using the IPF representation.

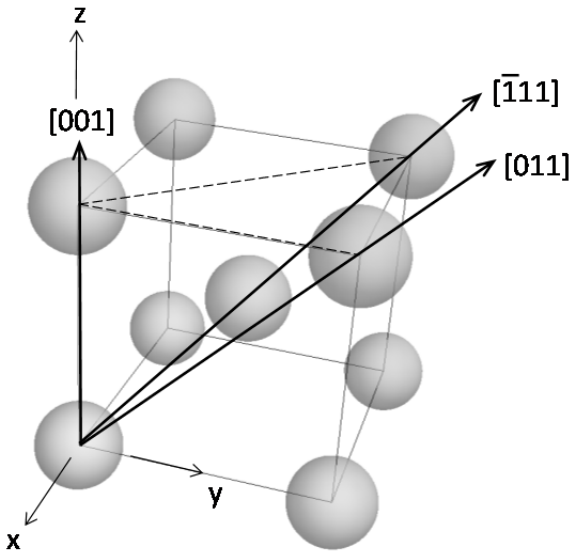

Figure 1.2- BCC unit cell illustrating bounding principle directions and triangular region used to define an IPF.

Figures 1.3 and 1.4 depict both α and γ-fiber textures using IPF's of the **RD** and **ND** axes. Figure 1.3(a) illustrates a concentration about the [011] direction (or pole) indicating that the **RD** axis is aligned near a ⟨110⟩ crystallographic direction for a majority of grains in a rolled polycrystalline material. The figure illustrates the texture as a distributed intensity about that pole. Correspondingly, Figure 1.3(b) illustrates the distributed locations of the **ND** axis, which must be orthogonal to the **RD**, therefore constrained to reside along the [001]-[111] axis in the IPF. The contouring and shading approximate the visualization realized for an α-fiber texture measured from rolled BCC metal in the figure. Usually, in rolled BCC metals, the **ND** axis distribution is not uniform about crystallographic directions normal to the [011] pole, thus the observed α-fiber texture is a *partial fiber texture*. In fact, the **ND** axis distribution often exhibits concentrations near either the [001] or [$\bar{1}$11] pole. Figure 1-4 depicts the γ-fiber texture using the same **RD** and **ND** IPF's. The concentration of **ND** axis measurements distributed about the [111] poles is clear in Figure 1.4(b). The corresponding distribution of **RD** measurements along an axis of crystallographic directions normal to the [111] pole ([011]-[112] axis on the IPF) is illustrated in Figure 1.4(a). The α- and γ-fiber texture do overlap in the IPF representation, thus this representation does not allow one to easily distinguish each texture component in a rolled polycrystalline BCC metal.

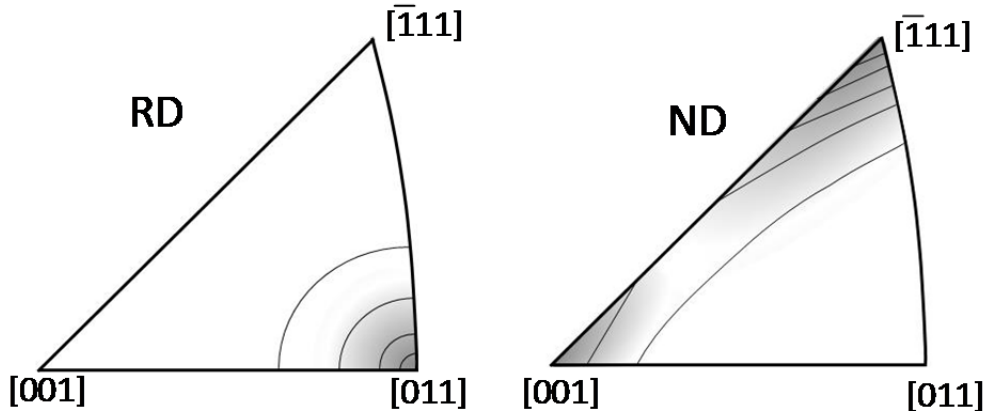

Figure 1.3- Depiction of α-fiber texture using IPF's.

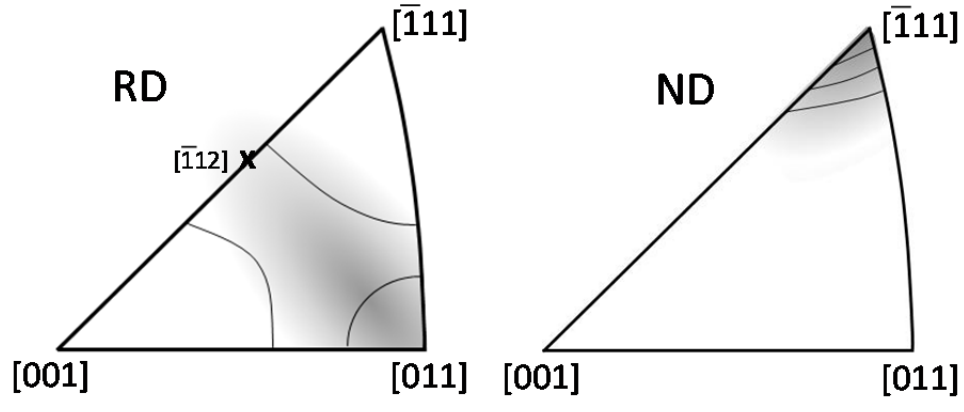

Figure 1.4- Depiction of a γ-fiber texture using IPF's.

Pole figures (PF) are used to graphically represent a family of crystallographic directions (or poles) within a globally defined space. Figure 1.5 illustrates idealized renderings of pole figures related to the textures observed in rolled Ta, or more specifically, the observed crystallographic texture in the DOE Tri-lab plate. Conventionally, in the case of interpreting crystallographic texture relative to a rolled plate, the normal axis to the {100}, {110} and {111} families of crystallographic planes (in cubic crystals these are equivalent to the ⟨100⟩, ⟨110⟩ and ⟨111⟩ families of directions) are plotted relative to a global space defined by the **RD**, **ND**, and **TD** axes of the plate, defined previously in Figure 1.1. The pole figures are projected hemispheres on to a plane (using a mathematical construction similar to an IPF), resulting in circular plots such as those shown in Figures 1.5. Also identical to the IPF representation, either area or angles can be preserved in a projection from hemisphere to plane in a PF. The center of the projected hemisphere is the **ND** direction and the **RD** and **TD** directions lie along its edges as defined in Figure 1.5.

Symmetry of a cubic crystal lattice dictates that there are three ⟨100⟩-type (i.e., [100], [010] and [001]), six ⟨110⟩-type and four ⟨111⟩-type directions, and a pole figure for each family of directions (or planes) will show intensities for each direction within a family. For example a *(100) pole figure* of a cubic crystal lattice, co-aligned with the global axis, will have intensities on a pole figure shown in Figure 1-5(a). One ⟨100⟩ direction is aligned with the **ND** axis revealing an intensity at the center of the pole figure and the other two- ⟨100⟩ directions are aligned with the **TD** and **RD** axis, but split on to either side of the hemisphere. A perfect crystal would be represented by single points on a pole figure whereas the rendering in Figure 2.4(a) represents a more realistic distribution of intensity about those ideal points. [10]. Envisioning a polycrystalline material with one ⟨100⟩ axis preferentially co-aligned with the **ND** direction, partially constraining the possible locations of the other two ⟨100⟩ axis leads to a pole figure illustrated in 1-5(b). In this rendering, intensities from the other two ⟨100⟩ are evenly spread within a ring defined by the plane containing the **TD** and **RD** directions, and therefore normal to the **ND** direction. This represents a complete ⟨100⟩ fiber texture aligned normal to the plate rolling direction, i.e. the **ND** direction. Variations of intensity within the ring in a real PF, indicate a partial ⟨100⟩ fiber texture. Similarly, Figure 1.5(c) is a rendering of a *(111) pole figure* illustrating a complete ⟨111⟩ fiber texture aligned normal to the plate rolling direction, a γ-fiber texture. One ⟨111⟩-type pole is constrained to be aligned with the **ND** direction. In this case, the angle between the constrained ⟨111⟩-type pole and the other three poles in the ⟨111⟩ family is fixed to 54.7°. Consequently, a ring of intensity is found at this angular distance as illustrated in the figure. Variations in intensity within this ring indicate a partial fiber texture.

The nomenclature for defining rolling textures in polycrystalline metals is to specify a crystallographic plane aligned with the rolling plane (normal to **ND**) and the crystallographic direction aligned with the **RD**. Intensities generated by the six ⟨110⟩ poles for idealized (100)[011] and (111)[011] rolling textures, as bounding examples, are shown in Figure 1.5(d) and (e), respectively (intensities occurring along the edge of a PF are split). Concentric rings encompassing the peak intensities are drawn on the figure to illustrate how these idealized textures translate to a α-fiber texture aligned with the **RD** using a *(110) pole figure* representation. A complete α-fiber texture would be evidenced by a uniform intensity within the rings. Correspondingly, a partial α-fiber texture is shown by varying intensity within the rings.

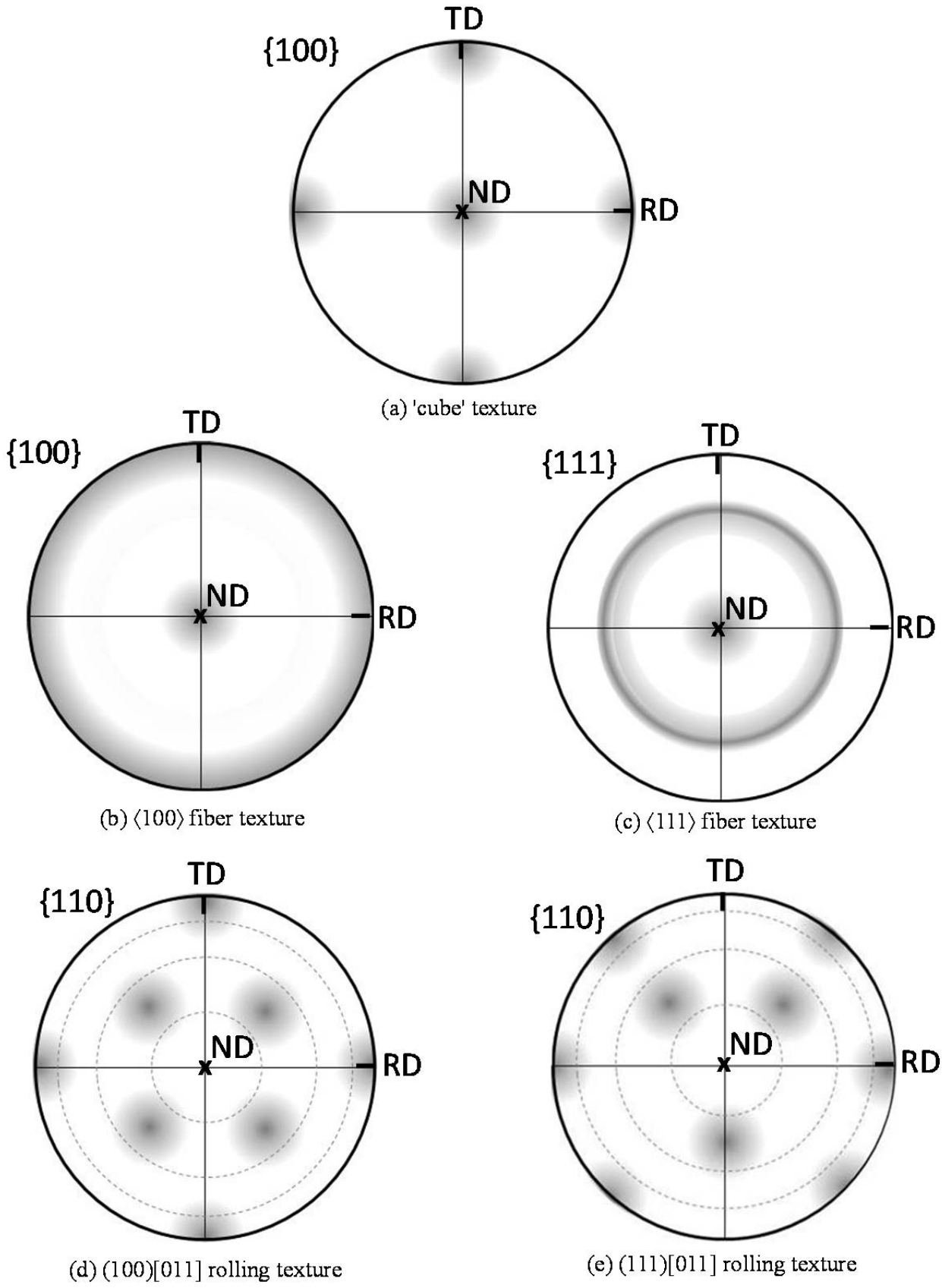

Figure 1.5- Illustrations of crystallographic textures observed from rolled BCC metals

Using rolling texture nomenclature, commonly observed textures for uni-directional rolled or rolled+annealed BCC metals span the {111}⟨110⟩, {112}⟨110⟩ and {001}⟨110⟩ components. [4] Plate center to surface texture gradients [12] [8] and significant microstructural banding during rolling also tends to occur in BCC metals, Ta is no exception to this; bands of grains with the ⟨100⟩ and ⟨111⟩ crystallographic direction aligned with the plate normal direction are often observed. [11] Although the Tri-lab plate exhibits excellent uniformity for a polycrystalline BCC material, it does exhibit crystallographic texture and a small degree of heterogeneity through the thickness and radially within the plate. Both of which are detailed in section 3 of this report, primarily through the use of electron back-scattered diffraction (EBSD) techniques. Interpretation of EBSD based microstructure mapping relies on characterization of crystallographic texture. This report restricts presentation of crystallographic textures to PF and IPF representations because they are easier for a reader not thoroughly familiar with crystallographic texture to interpret.

2. MICROSTRUCTURE CHARACTERIZATION

2.1 Through Thickness EBSD Characterization

Microstructural characterization of the DOE-tri-lab plate was performed utilizing scanning electron microscopy (SEM), focusing primarily on electron backscatter diffraction (EBSD) mapping. EBSD is a powerful microstructure characterization technique permitting detailed characterization of the crystallographic texture, banding, and other local microstructure variation information within a material. Results are typically assembled into maps colorized by crystal orientation referenced to a globally defined axis using an IPF legend [8]. Examples of EBSD maps of the microstructure of Ta plate are given in Figure 2.1. They are colorized using the legend shown in the figure, referencing the crystallographic axis to the plate normal direction for each measurement. For example, a grain within the polycrystalline microstructure oriented such that its ⟨111⟩ axis is coincident to the plate normal direction (**ND**) is colored blue, whereas a grain oriented with its ⟨100⟩ axis oriented coincident to the **ND** is colored red. Orientation banding is characterized by bands of grains with the same color in the EBSD maps. Figure 2.1 shows through thickness EBSD maps of (a) a vintage Ta bar obtained by LANL, (b) previously procured Ta plate not fully optimized for uniformity and (c) the center of a DOE Tri-lab plate. Microstructure heterogeneity and orientation banding in the vintage bar is evident. Although mitigated in the recrystallized microstructure observed in the later generation 'Previous Plate' shown in Figure 2.1(b), banding is still evident. Comparing Figure 2.1(c) to (a) and (b) offers a clear demonstration the superior uniformity of the polycrystalline microstructure in the Tri-lab plate. Achieving such a high degree of uniformity in the microstructure through the thickness of

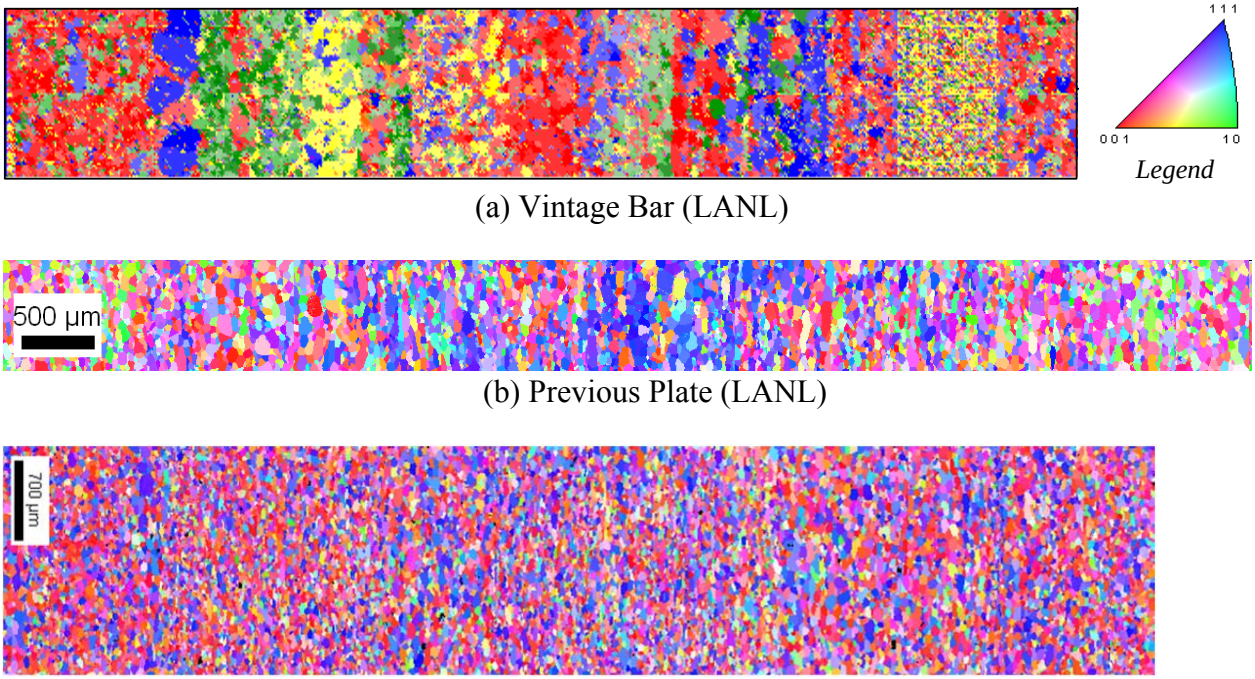

(a) Vintage Bar (LANL)

(b) Previous Plate (LANL)

(c) New DOE Tri-lab Plate

Figure 2.1 – Ta plate through thickness cross section EBSD maps.

a BCC polycrystalline metal plate indicates a carefully engineered process. An inherent expectation of such a microstructure is uniform mechanical properties through the thickness of the plate. However, a goal of this report is to document observed heterogeneity in microstructure and properties throughout a plate and between plates after characterization by both laboratories, LANL and SNL. Thus, the remainder of this section is devoted to characterizing the degree of microstructure variability within the Tri-lab plate and how it may manifest in local variation of plate properties.

The EBSD map shown in Figure 2.1(c) is composed of individual measurements with a 5 um spacing. It is a map of a 2 mm wide through-thickness section from the center of the plate, and represents an assembly of approximately 810,000 pixels. Each pixel is a measurement of the local crystallographic orientation, thus the entire map is an example of a rich quantitative dataset, which can be analyzed for evidence of microstructural inhomogeneity and crystallographic orientation banding. An analysis of the map in quartile sections is shown in Figure 2.2. ⟨100⟩ and ⟨111⟩ PF's, derived from the EBSD data, are shown for each quartile section in the figure. With intensities in the center of each, both PF's reveal respective ⟨100⟩ and ⟨111⟩ fiber textures aligned with the plate normal direction (**ND**). For comparison, idealized depictions of both fiber textures are given in Figure 2.4(b) and (c). Within the EBSD map the grains colorized red contribute to the ⟨100⟩ fiber texture component and the grains colorized blue contribute to the ⟨111⟩ fiber texture component. Nearly all grains in the map are colorized red or blue indicating that they contribute to one of the two texture components. The small percentage of grains that are neither red nor blue could possibly contribute to a minor texture component masked by the two identified fiber textures. More likely these grains represent a random component to the crystallographic texture distribution.

Figure 2.2 shows variations in intensity within the rings in the PF's indicating that the fiber components are *partial* rather than *complete* fiber textures. Because both ⟨100⟩ and ⟨111⟩ orientation families have directions perpendicular to a ⟨110⟩ pole, constraints imposed by an α-fiber texture encourage the ⟨100⟩ and ⟨111⟩ orientation preferences in the **ND**. The observed result would be specific intensities within the rings shown in Figure 2.2, similar to the illustrations shown in Figure 1.4 (d) and (e). While intensity variation does exist within the rings defined by the fiber texture components, the PF's in Figure 2.2 reveal evidence of the impact of clock-rolling the Ta plate to its final condition. This effectively spreads the uni-directional rolling texture component, the α-fiber, within the plane of rolling. Even though the resultant fiber texture components observed in Figure 2.2 are not *complete* fiber textures, randomization of the in-plane texture component is vastly improved from what is typically observed in rolled and annealed BCC metals. [4]

As mentioned at the end of the previous section, banding [11] and middle to surface through thickness texture gradients [12] [11] during rolling is endemic in BCC metals. Figure 2.1 reveals good examples of bands in the 'vintage' Ta bar. A reasonable first measure of banding or evidence of a plate middle to surface texture gradient is to quantify the ratio of ⟨100⟩ to ⟨111⟩ oriented grains within each quartile and note any significant changes in that ratio. Table 2. 1 lists those results for the Tri-lab plate and reveals only a small amount of variability in that ratio. It does reflect a slightly higher ratio in the top and bottom quartile sections (1 and 4) when compared with the middle quartile sections (2 and 3). This same slight texture gradient through the thickness of recrystallize Ta plate, where grains near the surface of the plate have a preferred

<100> orientation normal to the plate rolling direction and grains near the middle of the plate have a preferred <111> orientation, has been previously observed. [12] Another important measure of microstructural banding can be assessed by examining variation in grain size. In this case, grain size was also computed, from each quartile section of the EBSD map. Table 2.1 reveals a minimal variation amongst the four quartile sections for this parameter.

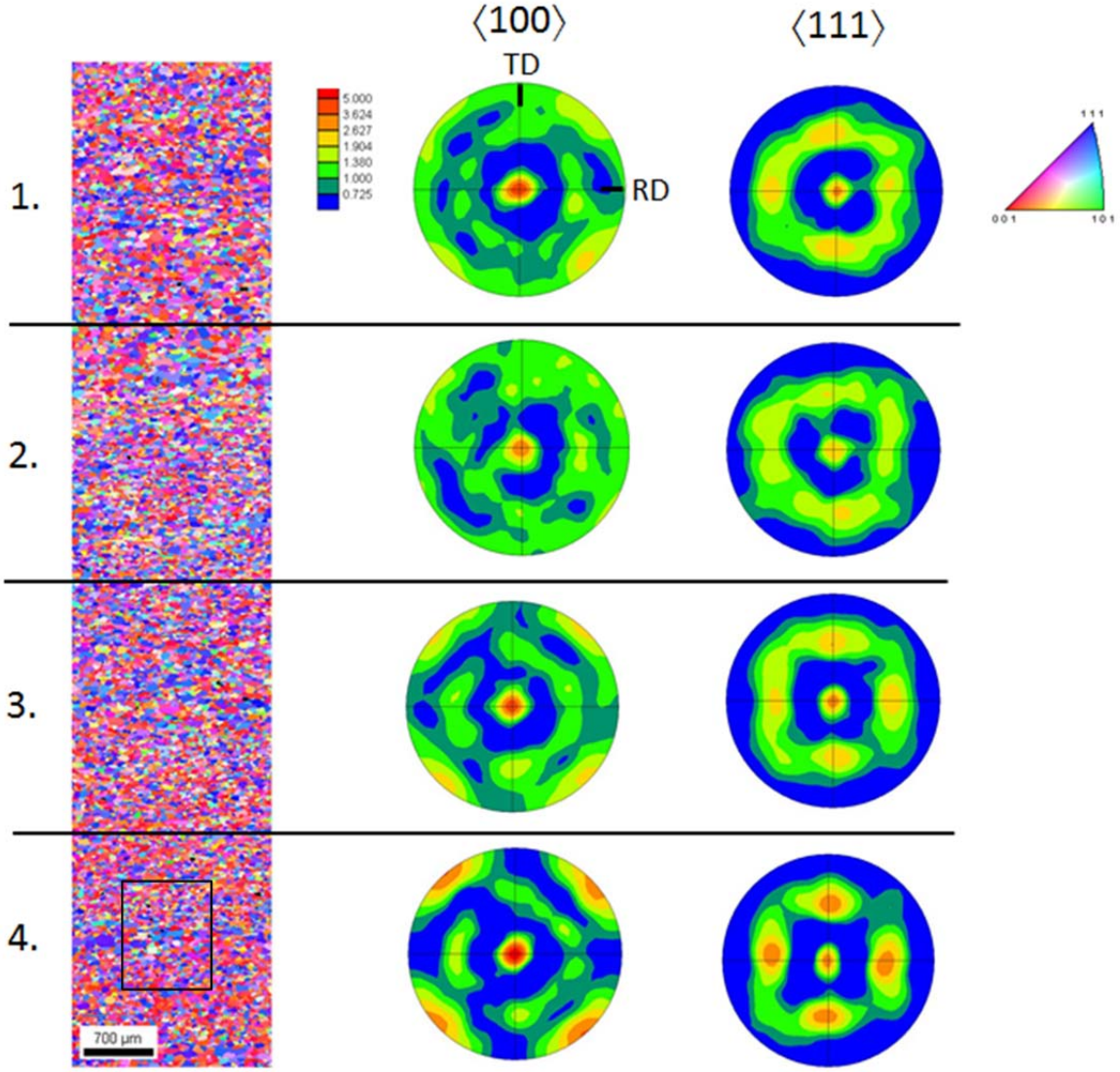

Figure 2.2- EBSD map of through thickness cross-section analyzed in quartiles.

Table 2.1 Results from Quartile Analysis

Quartile	⟨001⟩ /⟨111⟩ ratio	Grain Size (µm)
1	1.24	38
2	0.957	36
3	1.05	35
4	1.39	34

2.2 In-Plane BSE Imaging

SEM backscatter electron images (BSE) of metallographically prepared sections orthogonal to the **RD**, **TD** and **ND** plate directions are shown in Figure 2.3. BSE images reveal microstructure through different contrast between grains with different crystallographic orientations in a polycrystalline sample. Even small changes in orientation cause significant contrast changes. The images are placed in a cube configuration to clearly illustrate their orientation relative to the plate orientation. Each 'cube' shows a series of top and middle sections from the center and end of the plate. Recalling that the plate is clock-rolled, **RD** is the last pass rolling direction of the plate, the images reveal the expected recrystallized polycrystalline microstructure as well as microstructural differences dependent on location within the plate. The difference in grain size between the center and end of the plate is evident. The images from the center of the plate, figure 2.3(c) and (d) reveal contrast between the grains, as expected in BSE images. The individual grains are very distinct with each grain revealing a consistent non-varying shade of gray. Images from a location near the surface of the plate, figure 2.3 (a) and (b), similarly reveal contrast between grains but they also reveal contrast variation within grains. Arrows highlight a few grains with varying contrast in the images. This intra-granular contrast variation suggests subtle distortion of the crystallographic microstructure within grains and provides evidence of a degree of stored work in these regions.

2.3 Higher Resolution EBSD maps

Higher resolution EBSD maps, relative to those provided in Figures 2.1 and 2.2, were generated to quantify the variation in grain size that was observed in figure 2.3 between the plate center and end. They also provided an independent measure of any variation in crystallographic texture in those two locations, as well additional information regarding microstructure variability, such as subtle evidence of banding within the polycrystalline microstructure. Results are shown in Figure 2.4 for maps taken from the center of the plate and Figure 2.5 for maps taken from the end of a plate. The resolution of the maps, with a 1 μm step size is significantly higher than the through thickness map shown in Figures 2.1 and 2.2 but a significantly smaller region of the sample is mapped in each case. The box illustrated on the map in quartile 4 in figure 2.2 scales the maps shown in figures 2.4 and 2.5 to the through thickness section captured in that figure. The samples, and therefore the maps, were aligned with the last pass rolling direction of the plate. Each figure has two parts, Figures 2.4(a) and 2.5(a) are from a location near the surface of the plate and 2.4(b) and 2.5(b) are from the center of the plate. Thus, the two figures represent a total of four datasets.

In Figures 2.4 and 2.5, two maps extracted from the same dataset are shown for each case. The first, labeled **ND**, is referencing each orientation measurement to the plate normal direction. This is identical to the renderings presented in the through thickness map shown in Figure 2.2. The second map, labeled **RD**, is referencing each orientation measurement to the last pass rolling direction of the plate. Many features of the higher resolution **ND** maps are similar to those observed in the through thickness map. A majority of grains are red or blue, reflecting the crystallographic texture intensities in the ⟨100⟩-type and ⟨111⟩-type directions. Many of the grains are colored green in the **RD** map, delineating the α-fiber component (⟨110⟩ aligned with the last pass rolling direction) in the crystallographic texture. Corresponding IPFs are also shown in Figure 2.4 and 2.5 illustrating a measure of ⟨111⟩ and ⟨100⟩ crystallographic orientation

alignment with the plate normal (**ND)** within each mapped region. Recall that preferential alignment of the ⟨111⟩ and ⟨100⟩ crystallographic orientations to the plate normal direction (**ND**) is common in rolled and annealed BCC metals and this measure was performed on quartile sections in the dataset shown in Figure 2.2 and presented in Table 2.1. That result suggested some minimal microstructure variation through the plate thickness. It provided evidence of a slight middle to surface texture gradient but otherwise no crystallographic banding or any distinguishing localization of microstructural features beyond microstructure variability expected in a polycrystalline material. In these higher resolution results shown in figures 2.4 and 2.5, the IPF's confirm a local variation of ⟨111⟩ and ⟨100⟩ intensities with the ⟨100⟩ intensity clearly larger in the near surface maps, figures 2.4(a) and 2.5(a), and the ⟨111⟩ intensities clearly larger in the near middle maps. To further quantify this texture variation, Table 2.2 lists the ⟨100⟩/⟨111⟩ intensity ratios at the poles as a comparison with the quartile results given in Table 2.1. The ratios in Table 2.2 are more disparate than the comparable measures given Table 2.1 (middle to quartile 2 or 3 and top to quartile 1 or 4) possibly because of the more localized sampling of data used to compute the ratios in Table 2.2. With regard to the higher resolution regions mapped, in both cases, center and edge the <001>/<111> ratio actually 'flipped' when comparing the middle to near surface locations. That is, the <111> intensity was greater in the middle of the plate and the <001> intensity was greater near the surface of the plate. Similar texture gradients, where <001> oriented grains relative to the plate ND are favored near the surface of a Ta plate, has been previously observed. [12]

The BSE images that compose figure 2.3 already establish that the grains are larger near the end of the plate. Table 2.2 also includes quantitative information regarding grain size and grain aspect ratio extracted from the EBSD datasets composing the maps in figures 2.4 and 2.5. The values indicate that the avg. grain size has increased by approximately factor of 1.5-2 and the grains are slightly more equi-axed near the end of the plate. Correspondingly, both the <001> and <111> texture components have higher intensities near the end of the plate. Assuming that a larger grain size corresponds with more grain growth, this correlation suggests the <001> and <111> grains have a propensity to consume grains with other orientations during a heat treatment (a process which encourages grain growth) resulting in a sharping of these texture components near the end of the plate.

Also given in Figure 2.4 and 2.5, is a ⟨110⟩ pole figure for each case. These were provided to illustrate the α-fiber crystallographic texture component generated by rolling of the plate. Clock-rolling is expected to spread this component within the plane of the plate, although that may not be evidenced in this depiction of crystallographic texture. As reviewed in section 1, a complete α-fiber texture would exhibit concentric rings in the PF's given in the figures and a partial fiber texture would exhibit partial rings or rings of varying intensity. Both the PF's and the **RD** EBSD maps show that a large percentage of the grains have ⟨110⟩ crystallographic axis aligned with the last pass rolling direction. Intensity variations within the concentric rings are evident in the PF's in figure 2.4 from the end locations indicating non-uniformity or tending toward a partial fiber texture at these locations. More uniform intensity within the rings at the center locations reflect a more nearly uniform fiber texture at these locations. As expected, the degree of uniformity in the <110> fiber texture component in the plane of rolling correlates with the sharpness of the <001> and <111> components exhibited in the **ND**- IPF's.

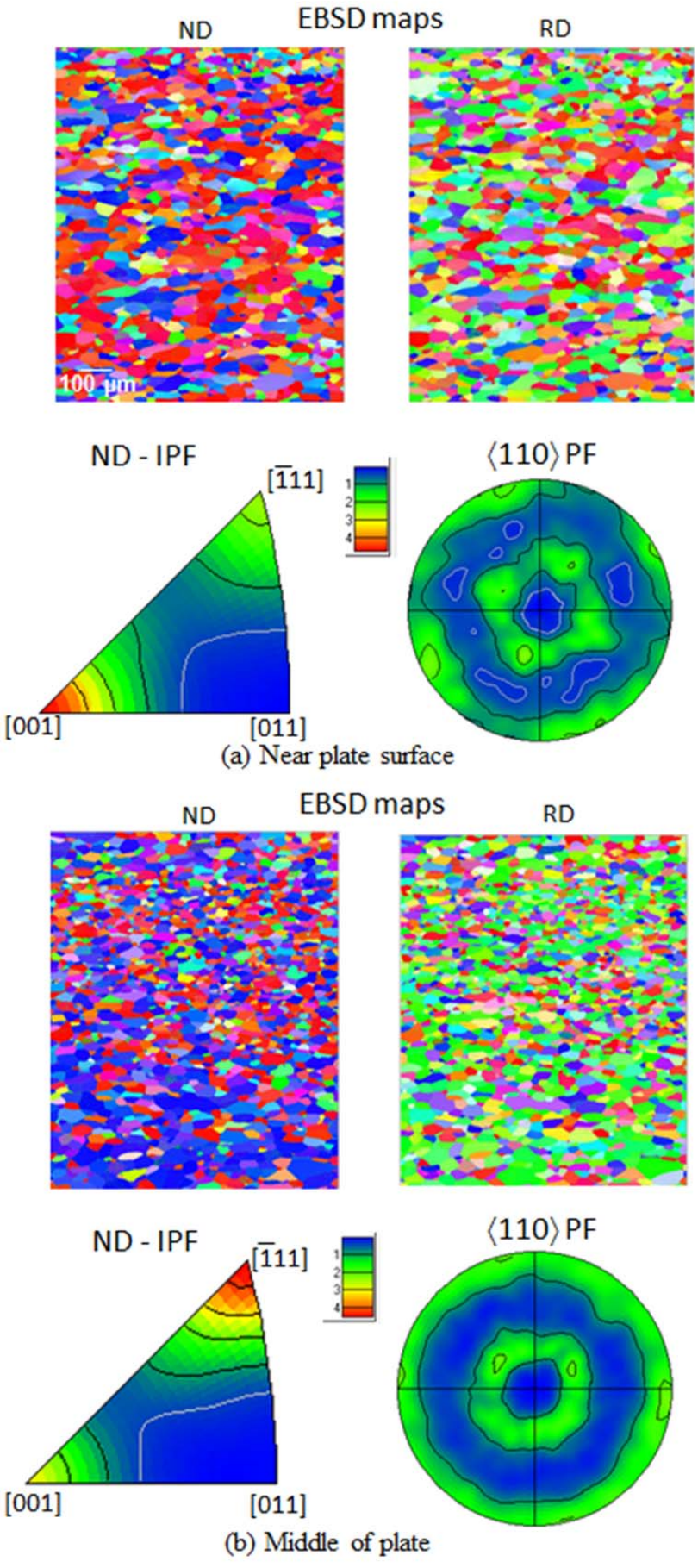

Figure 2.4- Higher resolution EBSD maps from the *center* of the plate, referencing the microstructure to the plate **ND** and **RD** with corresponding <110> PF's and an IPF's referenced to the plate **ND**.

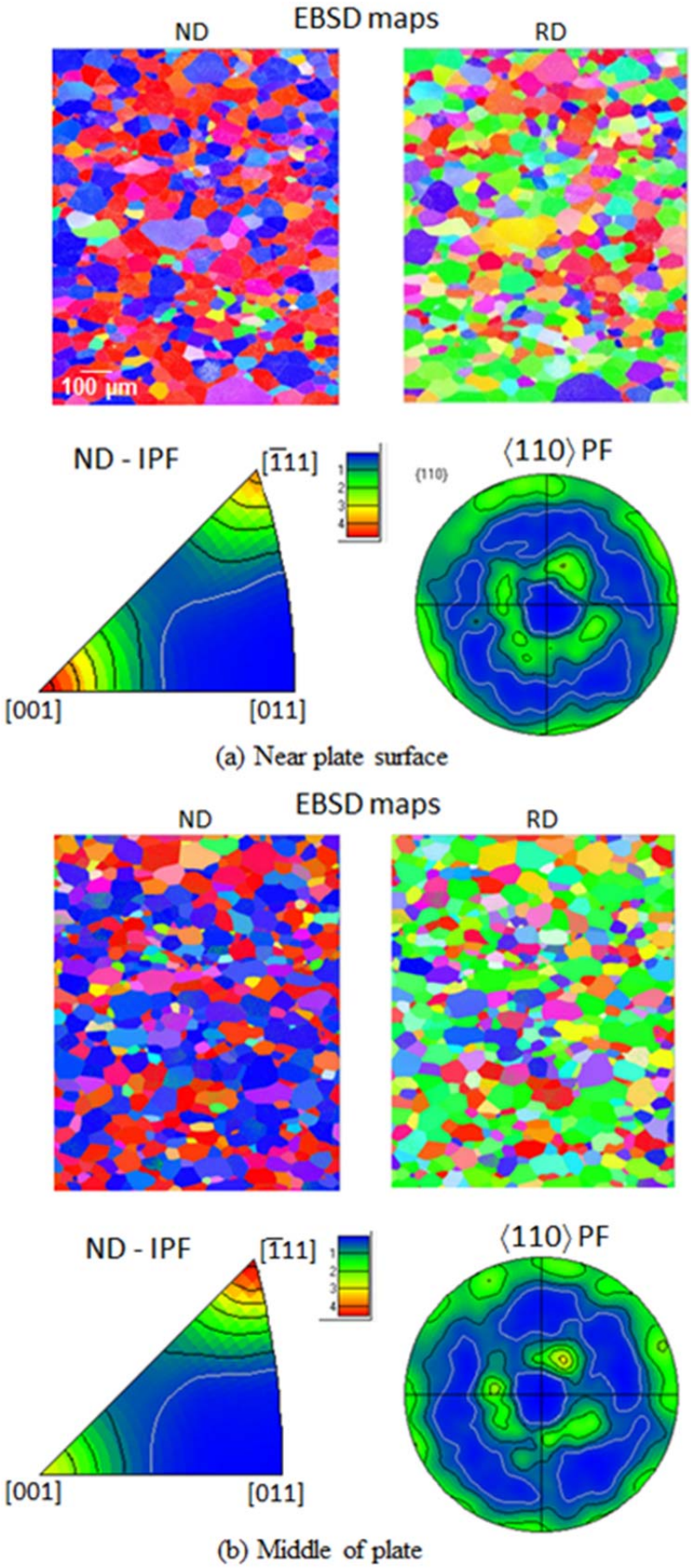

Figure 2.5- Higher resolution EBSD maps from the *end* of the plate, referencing the microstructure to the plate **ND** and **RD** with corresponding ⟨110⟩ PF's and an IPF's referenced to the plate **ND**.

Table 2.2 Microstructure Statistics from Higher Resolution Maps

Location	⟨001⟩/⟨111⟩ ratio	Grain Size (μm)	Aspect Ratio
Center Top Edge	3.99/2.17 (1.83)	27.1	1.63
Center Middle	2.89/4.29 (0.67)	23.7	1.60
End Top Edge	5.16/4.07 (1.26)	38.3	1.12
End Middle	3.87/6.00 (0.64)	39.7	1.07

3. MECHANICAL PROPERTIES

3.1 Tension and Compression Testing

3.1.1 Sample Geometry and Test Procedures

Bulk mechanical testing, to date, has primarily consisted of a series of tension and compression tests designed to characterize plate-to-plate variation, and directional, in-plane and through thickness property variations of the Ta Tri-lab plate materials. Most compression test cylinders were machined from plate #19212 to a 5mm diameter and a 5mm height and tested at LANL. These serve to examine the variation of properties within a single plate. However, one series of compression specimens was extracted from plate #19206 (furnished by SNL) to complete a plate-to-plate comparison experiment. The cylindrical compression test sample is a preferred test geometry because it readily lends itself to both quasi-static and high strain rate testing. Specimens were machined such that the compressive axis was oriented with (1) the normal of the plane of the rolled plate – through thickness (TT), (2) the final rolling direction pass – in plane A (IPA), and (3) orthogonal to both the TT and IPA directions (IPB). This was done to examine the role of plate texture. The TT direction aligns the compression test axis with the crystallographic texture component along **ND** axis and the IPA direction aligns the compression test axis with the crystallographic texture component along the **RD** axis. Next, specimens were also machined from differing radial positions within the plate: center, mid and edge to sample for any radial variation in the plate properties. TT, IPA, IPB, center, mid, and edge locations are indicated in Figure 3.1. All of the compression test results are included in the next subsection.

Tension testing was carried out at SNL utilizing a flat, dog-bone shaped, tensile coupon geometry. These specimens were machined for plate #19206. Most of these tests used tensile coupons with a ½ scale version of the ASTM E08 standard [13]. Thickness of the coupons was 0.063" or 1.6 mm. A key purpose of the small geometry was to sample small enough volumes to capture any local property variations within the plate, especially with regard to through thickness variations as this geometry allowed for 3-5 identical samples to be machined through the thickness of the plate with the tensile axis aligned along the IPA or IPB directions. This is shown in Figure 3.2. Starting from the top-side of the plate, each sample is equally spaced though the thickness, within the limits of electro-discharge machining. To address any concerns associated with testing samples outside the geometry envelope defined in ASTM E08, one additional set of three samples (LCL samples) were fabricated to dimensions exactly specified for a sub-sized specimen and tested for comparison.

Both compression and tension experiments were performed at room temperature and a strain rate of 0.001/s, well within the quasi-static regime. Figure 3.1 is a layout of the locations of where the various samples were extracted within a plate. Sub-size (half) tension test locations are designated by (a),(b),(c) and (d) in the figure. The location of the larger ASTM E08 subsize samples is also indicated. Finally, the locations where the microstructure characterization samples were located, whose results were detailed in the last section, are also identified as *MIDDLE* and *EDGE* in the figure for reference.

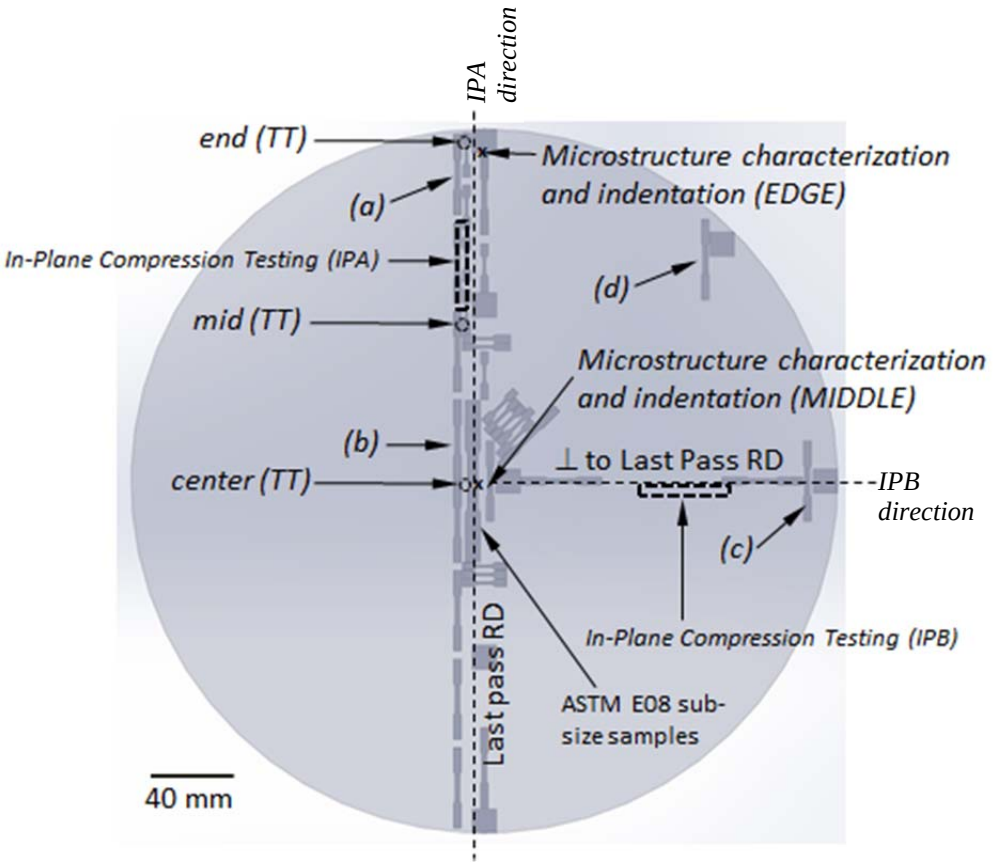

Figure 3.1 Map of extraction locations from Ta plate for tension and compression test samples.

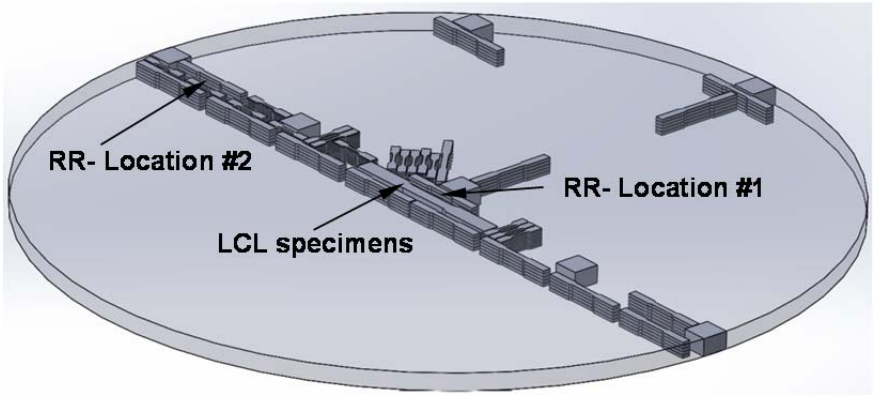

Figure 3.2 Isometric view showing how tensile bars were machined the through thickness section of a plate.

3.1.2 Quasi-static Compression Testing Results from within a Single Plate

All compression and tension test results are presented as true stress-true strain curves, allowing for more direct comparison of results from different data sets. In the case of the compression tests, initial results from a series of TT compression testing experiments, shown in Figure 3.3, suggested radial variation in mechanical properties. The results are shown as a series of stress-strain curves from center, middle, and end plate locations. Indicated on figure 3.1 as center (TT), mid (TT) and end (TT), the axis from which these samples were extracted lies along the last pass rolling direction. Duplicate tests were performed in each region and good repeatability was found in the center and mid regions, so for clarity sake, only one test is shown for those regions in Figure 3.3. Some variability was observed in specimens tested in the edge region, as such the data from more than one test in that region is provided in Figure 3.3. From these data, the yield stress is observed to vary by as much as 50 MPa as a function of radial position within the plate. These data suggest a relatively similar work hardening response after the initial yield as a function of radial position within the plate. The increase in yield stress associated with specimens approaching the edge of the rolled plate may be rationalized in terms of the texture variations quantified in Table 2.2. Through thickness (TT) variations in texture may trend with plate radius. Specifically, while there is a larger ⟨001⟩ component in the center of the plate (by radial distance) than at the end of the plate, this difference is more substantial if one compares the ⟨001⟩/⟨111⟩ ratios measured at the top edges in these radial locations rather than using the middle sections. Whether comparing top edge or middle through thickness locations, the ⟨111⟩ component is stronger in the end as compared to the center. In these compression tests, the averaged response of both locations yields the macroscopic properties measured in the test. As such, the enhanced ⟨111⟩ texture in the end specimens is likely to decrease the activation of slip due to less planes with high Schmid factors (oriented favorably for slip-based deformation) being available during deformation as compared to the specimens in the center of the rolled plate. [12][14][15] These data and this interpretation guided subsequent experiments, conducted at both SNL and LANL, as to specimen location and further data analysis.

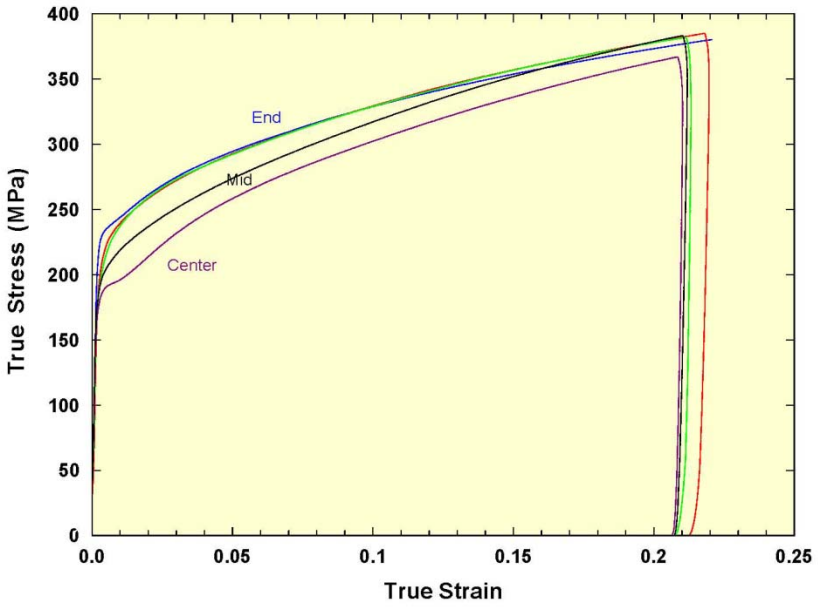

Figure 3.3 – Through thickness (TT) compression testing along last pass rolling direction.

Figure 3.4 represents the next series of experiments, intended to provide a more complete characterization of the rolling texture impact on the directional mechanical response of the Tri-Lab plate. To this end, TT, IPA, and IPB compression specimens were tested from the center and mid-radial regions of the plate. While again numerous tests were performed to establish data repeatability, for clarity sake only two samples from each location are shown in Figure 3.4. These tests reveal a degree of variability as a function of rolling texture (through thickness (TT) vs. in-plane (IP)). Additionally some scatter associated with observed yield strength is observed in IPA and IPB specimens. The post-yield work hardening response was nearly identical for all specimen directions.

Finally, a comparative series of large-strain, compression experiments were performed on TT samples at the center and end plate locations. These tests were performed to ensure that differences in mechanical response as a function of radial location within the plate persisted to large strains and the data is given in Figure 3.5. The experiments were performed not in one single loading of the specimen but in load/reload cycles to ensure that specimen compression surfaces remained well lubricated. Also, as a comparison to previous Ta material, Figure 3.5 includes a similar high strain test result for a compression specimen from another plate of Ta, called DOD-DOE Ta. The microstructure of this material is shown in Figure 2.1(b). This specimen was also tested in the TT direction. Results in Figure 3.5 show that the relatively low strain behavior observed in Figure 3.3 persists to high strains shown in Figure 3.5. Additionally, the relatively quick return to anticipated flow stress levels (flow stresses realized prior to unloading) upon reload, suggests that adiabatic heating does not contribute significantly to the high strain response of the current Tri-Lab material or the DOD-DOE material under quasi-static loading conditions.

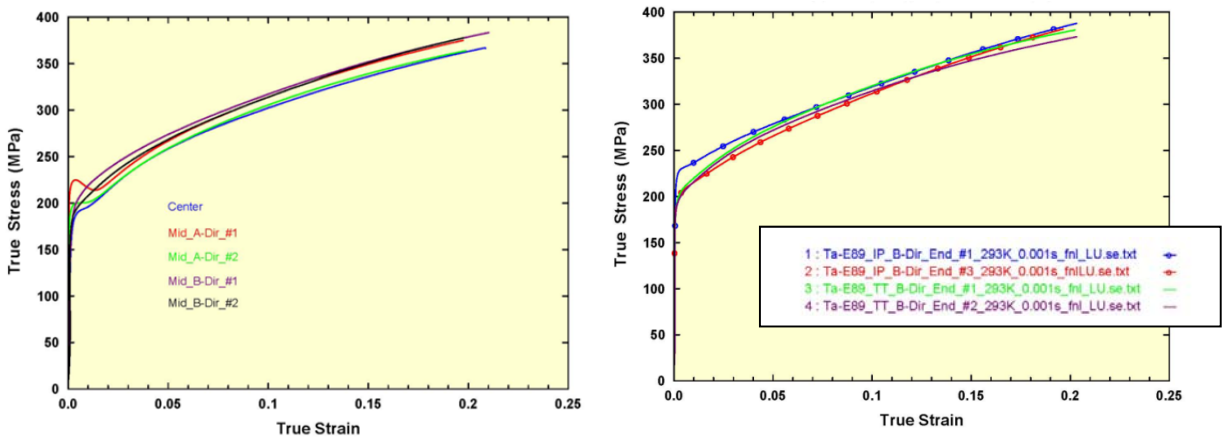

(a) (b)

Figure 3.4 Compression test results from select locations and orientations within a plate. (a) Through thickness samples taken from axis aligned parallel and perpendicular to last pass rolling direction. (b) 'end' location samples with their test orientation aligned through the plate thickness (TT) or parallel to the last pass rolling direction (IPB).

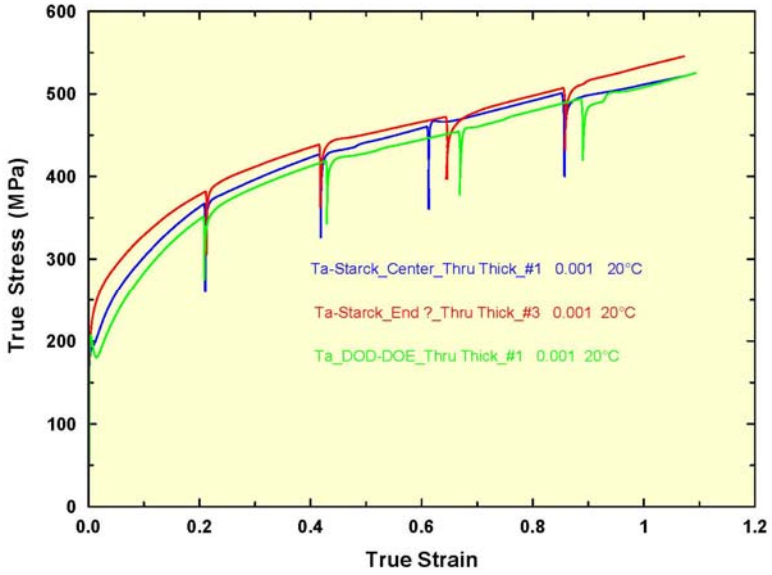

Figure 3.5 –Large strain compression testing results on through thickness (TT) compression cylinders taken from center and end plate locations.

3.1.4 Round Robin Compression Testing: Plate to Plate Comparison

A series of compression tests were conducted on samples taken from the center and end regions of each of the two plates (#19212 and #19206) and directly compared to characterize any plate-to-plate variability. These locations are given in Figure 3.2. These samples were in the IPA orientation and therefore parallel to the tensile specimen test axes for the data described in the next section. The data is given in Figure 3.6. In this case, some subtle variation in yield stress but little difference in the work hardening response is observed between results from the two plates.

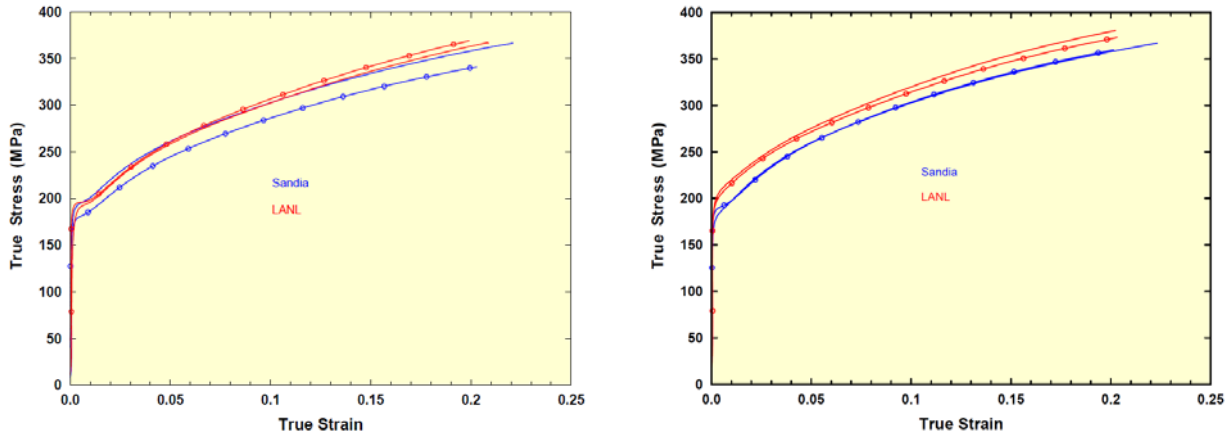

(a) (b)

Figure 3.6- Comparison of results from compression testing on two separate plates from (a) location #1 and (b) location #2. Both locations are indicated in figure 3.2.

3.1.5 Tension Testing Results

The first series of tension tests were performed on samples labeled LCL in Figure 3.2. Of the series of tensile samples extracted from the #19206 plate, the geometry of the three LCL samples, as many as could be extracted through the thickness of the plate, rigorously followed ASTM E08 subsize geometry specifications. Results from these samples were then directly compared to the ½ subsize sample, tensile tests which comprise the rest of the tension test results. Any difference would bring the validity of the results using the undersized sample geometry into question. In these tests, gage section displacement measurement was performed using a laser extensometer and clip extensometer. The laser extensometer did not have the resolution of the clip extensometer, but did have the range to measure displacement until the samples failed. Results from using both displacement measures are given in Figure 3.7, (a) using the laser displacement and (b) using the clip extensometer, respectively. Results in Figure 3.7(a) are plotted on an engineering stress vs. engineering strain basis because necking, as unstable plastic deformation, encompasses a portion of the curves and cannot be converted to a true stress-true strain basis. The results shown in Figure 3.7(a) indicate that the stress-strain curves saturate at approximately an engineering strain of 0.3 suggesting the onset of necking at this strain. The specimens sustained a stress nearly that of the ultimate tensile strength of about 250 MPa until at least a strain of 0.5 was achieved. This suggests a diffuse, somewhat stable necking behavior, before a rapid decline in strength and final failure between a strain of 0.5 – 0.6. [16]

Measurement of displacement by either extensometer was indistinguishable on the scale plotted in Figure 3.7. For consistency and comparison with the compression tests, results using the clip extensometer were converted to a true stress vs. true strain basis and plotted to a strain of 0.2, well below the strain for necking, in Figure 3.7(b). From these data it is observed that yielding occurred approximately between 160-190 MPa. This spans the range defined by the compression tests performed on the same plate, shown in Figure 3.6. Stress-strain curves from both tension and compression experiments commonly show a sudden drop on yielding such that an upper and lower yield point can be defined. The tensile specimen geometry seems to

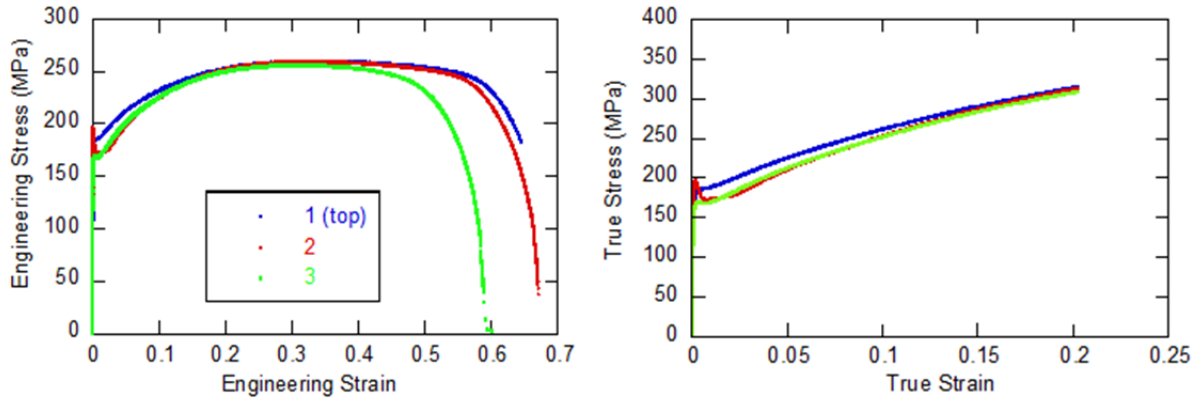

(a) (b)

Figure 3.7 Tensile test results from LCL samples. (a) Engineering stress vs. strain curves to failure. Strain determined from laser displacement measurement. (b) True Stress vs. True Strain curves to a strain of 0.2. Strain determined from clip extensometer.

encourage this yield point effect. The load drop observed upon yielding is common in BCC metals, including Ta and Ta alloys [17], but not addressed in more recent studies regarding modeling the mechanical behavior of Ta. [18][19][20] In part, because the load drop observed upon quasi-static yielding is not deemed a critical component of the predictive capability of models intended to capture dynamic response of Ta. [21][22][18][23] Historically, the yield point drop in Ta was investigated in the 1960's by Arsenault; it was tied to the influence of a rapid multiplication of mobile dislocations necessary for plastic flow. [24] Arsenault speculated solute (impurities) may have played a role, although the TriLab-Ta plate considered in this investigation is remarkably pure with low initial dislocation content. Thus, a rapid burst of dislocations to initiate plastic flow seems the most plausible mechanism as the reason for the post-yield load drop. Within the sets of compression and tension tests presented here, the post-initial yield load drop is not always observable and is variable across the different data sets, although load-drops by as much as 50 MPa after initial yield can be noted in the series of tensile stress-strain curves shown in Figures 3.7 and 3.8.

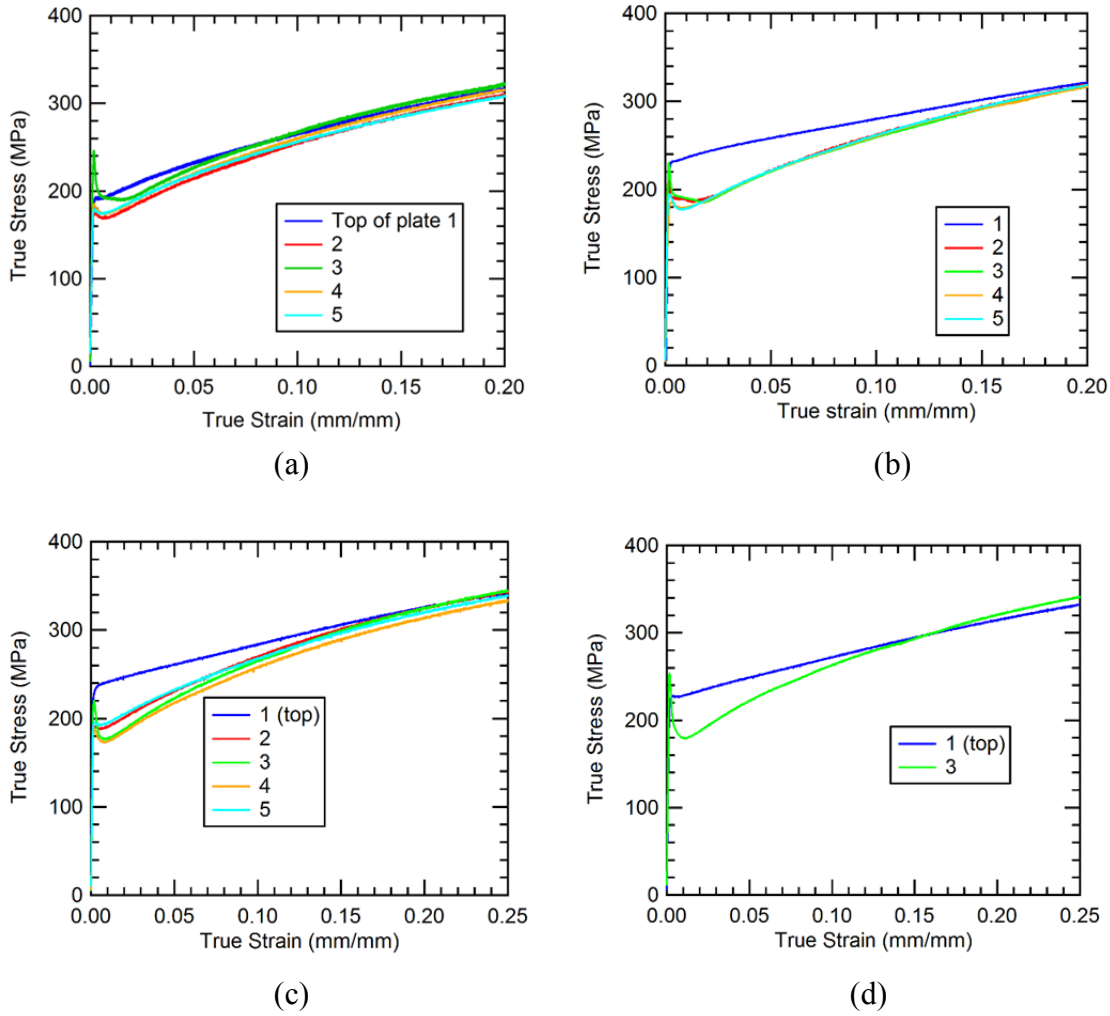

Figure 3.8 – Through thickness Tension Test Results at various locations in the plate.

Results from the ½ subsize samples taken from locations labeled (a), (b), (c) and (d) in Figure 3.1 are shown in Figure 3.8. At each location, five identical samples were tested. A sixth sample was machined at each location at the very bottom of the plate, but did not have the pre-defined requisite thickness dimension of 0.063" and was not tested. Thus, the five tests at each location represent a series of mechanical tests that interrogate the through-thickness mechanical properties of the plate in each of the five locations. Sampling of various radial positions in the plane of the plate was also accomplished through the four sets of tension test results. Sets (a), (c) and (d) were samples taken from positions near the end of the plate and set (b) was taken from a location near the center of the plate. The curves shown in Figure 3.8 are nearly identical to those in Figure 3.7(b) indicating that the scaled down test geometry did not adversely affect the measurement. Figure 3.8 (a), (b) and (c) show all five stress-strain curves for the series of five samples extracted though the thickness of the plate at each location. The legend in each figure specifies samples 1-5, where 1 represents a sample taken from the top of the plate and 5 represents a sample taken from near the bottom of the plate. Sample 3 is taken from very near the middle of the plate thickness. The variability in stress-strain behavior did not noticeably change amongst the individual data sets, (a), (b), (c) and (d) in Figure 3.8, indicating that there is little difference in the tensile mechanical response as a function of radial position in the plate. In fact, the stress-strain behavior between each radial location is remarkably consistent. Recalling that the compression experiments did reveal a trend with radial location in the plate can be attributing to the testing direction. Compression samples which exhibited the radial trend were aligned through the plate thickness (TT) whereas the tensile specimens were aligned with the plane of the plate (IP).

The consistently observed trend amongst all four of the datasets is that in each case sample 1 showed no load-drop after yielding and a slightly altered work hardening response. Only sample 1 and 3 were tested at plate location (d) and are included as Figure 3.9(d) to provide a fourth example of the difference regularly observed in the stress-strain response between center and top of plate specimens. Presumably, the flat geometry, size and location of these samples at the top of the plate allowed for them to capture the effect of a small additional amount of stored work in the material near the surfaces of the plate. The observation that a degree of stored work at the top and bottom of the plate eliminates the load drop on yielding in pure Ta lends plausibility to the rapid dislocation multiplication mechanism discussed earlier in this section.

3.1.6 Comparison of Compressive and Tensile Behavior

Figure 3.9 compares the range of compression test stress-strain curves with the LCL tension test results shown in Figure 3.7. From a continuum mechanics perspective, testing in tension and compression should produce identical true stress vs. true strain behavior. In this case, the experiments show that although yielding occurs within the same stress range for both experiments, the material work-hardens more rapidly in the compression experiments. In BCC metals, difference in tensile and compressive behavior, defined as tension-compression asymmetry, has been previously observed during yielding of single crystals. [25] Prevailing explanations for this behavior are related to the non-associative component of stress required to accomplish the mechanism of dislocation slip required for plastic deformation in BCC metals. [26][14] Classical experiments on Ta single crystals [27][28] document tension-compression asymmetry of yield, but not of the work-hardening response. Results on the polycrystalline Ta

samples given in this report suggest the nature of the polycrystalline Ta behavior at yield obviates the asymmetry classically observed in the single-crystalline response. Even loading along an axis with a different crystallographic texture does not generate a significant difference in the yield strength (Figure 3.4). Therefore, the origin of the different work-hardening response observed between tension and compression testing results is not yet clear. Two plausible explanations for the different work hardening behavior are:

i) Significantly different geometry of the test samples, the flat dog bone geometry of the tensile test coupons may have a slightly reduced constraint vs. the round cylindrical geometry of the compression cylinders, which may exhibit slight barreling during testing.

ii) Orientation hardening driven by the different evolving texture in compression vs. tension

Either explanation could be verified or ruled out with additional experiments and more detailed modeling but is beyond the scope of this report.

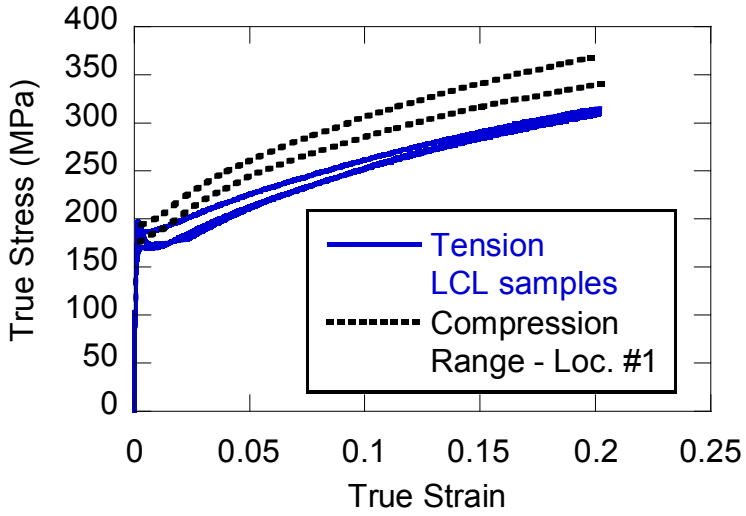

Figure 3.9- Comparison of Tension and Compression Stress-Strain curves.

3.2 Hardness Testing

Both microhardness and smaller scale instrumented indentation experiments were performed through the thickness of the Tri-lab Ta plate material to provide a local properties measurement in terms of material hardness. The measurement values are derived from the amount of force required to drive a pyramidal diamond tip into the surface of a material and the resultant penetration depth. The material underneath the tip experiences a multi-axial primarily compressive stress and strain state resulting in a measurement that is not particularly direction sensitive. Thus, it is not sensitive to crystallographic orientation dependent properties or tension-compression asymmetry. However, the measurements can be sensitive to changes in strength due to other microstructure variations in a material, such as variations in grain size and stored work. Microhardness testing was performed using a four-sided pyramidal tip, from which a measurement of the resultant impression provides a Vickers Hardness Number (VHN). The

microhardness test follows a standard procedure for conducting the experiments and reporting results. [29]

Instrumented indentation follows the same principle of pressing a pyramidal diamond tip into the surface of the material, but allows for a scaling down of the experiments to lower loads and depths by generating and evaluating a load-displacement trace of the experiment using an instrumented tester. Typically, a 3-sided, diamond, pyramidal tip is used and a measure of hardness and modulus can be extracted from the resulted load-displacement curve. [30] Methods for measuring hardness and modulus using instrumented indentation are also standardized. [31] Instrumented indentation hardness values are derived from a force over projected contact area between the tip and tested material, and they are typically reported in units of GPa. They can be related to microhardness values with the caveat that instrumented indentation results are sensitive to size-effects, tip bluntness, and pile-up of material around the impression during an experiment.

Both microhardness testing and instrumented indentation experiments were performed on the same cross-sectioned samples, taken from plate #19206, used for the microstructure characterization given in section 3.3. Middle and top locations from the cross-sections taken from the center and end of the plate were tested. The locations were chosen to provide a comparison and possible correlation in hardness measurements with the grain size between center and end sections (figure 2.3) and provide supporting details regarding the evidence of stored work near the surface of the plate.

3.2.1 Microhardness Testing

The microhardness testing was performed with a Struers Durascan hardness tester with an automated measurement capability. This tool allowed for setting a grid for indentation experiments from the metallographically prepared samples extending from the edge toward the center of the plate cross-section. At each experimental location, a 100 gram indentation load (0.98 N), was applied to the diamond tip stylus which left an impression that could be measured optically to determine the VHN. In relative terms, a material hardness measurement correlates to strength and stored work at that location. A grid of microhardness experiments can thus yield a relative measurement of local properties variations within a section of material.

A grid of experiments and a plot of the measured values on through thickness, cross-sections from the center and end of the plate are shown in the optical micrographs of Figures 3.10(a) and 3.10(c), respectively. Each grid extended from the edge to about 3.5 mm toward the center of the 10.38 mm plate thickness cross-section. The orientation of the cross-section is along the last pass rolling direction, identical to the plate cross-section shown in figure and defined by the coordinate system in the figure 1.1(b). To detect any change in hardness due to the possible presence of stored work near the edge of the cross-section, the grid of measurements was aligned to be parallel with the top edge of the cross-section and measurements were averaged by row. Each row contains 17-18 measurements and the rows extended to about 3.5 mm from the edge of the sample. Those measurements and the resultant average and standard deviation by row are plotted in figure 3.10(b) and 3.10(d), respectively. In each case, measurements from the row closest to the top edge of the sample were impacted by edge effects, specifically, the lack of constraint, lowering the measured hardness values. Because the first column in each sample is also very close to an edge, those measurements were excluded from the row averaged values

given in the plots. Both the impacted row and column for each set of measurements are indicated and enclosed by a gray box in 3.10(a) and (c). Otherwise, the plots show a distinct trend of increasing hardness extending toward the edge of the plate. Hardness values of about 90-95 VHN found toward the middle of the plate increased to greater than 100 VHN as the measurements approached the top of the plate. The increased hardness near the top of the plate is more pronounced in the center measurement (figure 3.10(a) and (b)) where the averaged hardness increased to over 110 VHN for the row of measurements within 0.5 mm of the top surface of the plate cross-section sample. An increase in measured near-surface hardness in both center and edge sections is evident and extends about 2 mm in from the top surface.

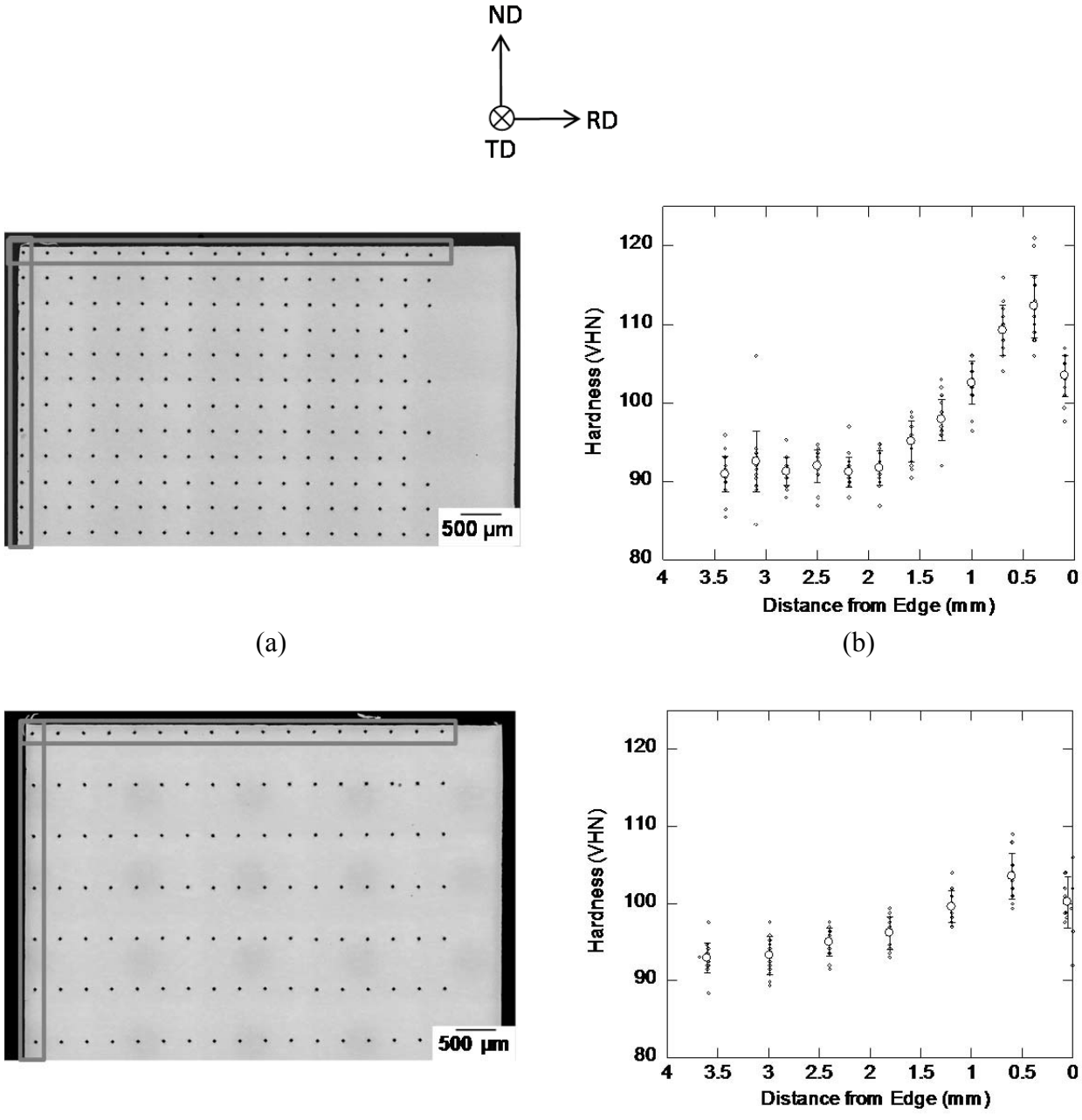

Figure 3.10 – (a) Grids of microhardness measurements extending from the edge toward the middle of a cross-sectioned sample taken from (a) the center and (c) the end of the Ta-plate. (b) and (d) plot the corresponding VHN results averaged by row. Near edge column and row measurements indicated by the gray boxes were influenced by edge effects. Near edge coumn measurements were not included in the averaged results.

3.2.2 Instrumented Indentation

Continuously collected load, displacement, and contact stiffness data allows for an extraction of measured hardness as a function of indentation depth throughout an instrumented indentation experiment. To compare with the microhardness experiments, a total of 16 instrumented indentation experiments were conducted at 4 locations, near the top (within 1 mm) and at the middle of the same through thickness center and end (radial) locations. In terms of load, the scale of the experiments is about 3 orders of magnitude smaller than microhardness tests. They were carried out to a depth of 250 nm, which required approximately only a 2 mN load. A 4x4 grid of experiments easily fits within a square whose corners are defined by four adjacent microhardness indents shown in Figure 3.10(a). Results are plotted in Figure 3.11(a) for the measurements taken from the middle section and in Figure 3.11(b) for the measurements taken from the end section. Each curve on both plots represents the average of 16 experiments as a plotted as function of indentation depth. Ideally, for the self-similar pyramidal tip geometry used in these experiments, hardness would be constant as a function of indentation depth. However, at shallow depths (<50 nm), tip bluntness and indentation size effects influence the measurement. These samples were metallographically prepared and mounted in epoxy. Compliance in epoxy mounted samples tends to impact the measured hardness values at depths exceeding 250 nm. Due to these considerations, an ideal range from which to extract hardness values from the measurement is between 50 nm – 250 nm. The plots in Figure 3.11 show that for Ta mounted in epoxy, perhaps 100 nm- 250nm is a more optimal range.

Both plots reveal a small but measureable increase in hardness found on the top of plate relative to the middle. The percentage difference from center to top, approximately 15%, corroborates with the percentage increase in the microhardness measurements as they approached the top of the samples. With regard to direct comparison of the measured values, accounting for experiment geometry only, a VHN corresponds to a hardness value measured in GPa when divided by 94.59. Thus hardness values measured by microhardness testing are low relative to those measured by instrumented indentation. Pile-up of material around the indentation, commonly referred to as indentation pile-up, typically occurs in soft metals. It influences the measured values using instrumented indentation significantly [32] and is the likely cause of the difference in absolute values in both measurements. The measured increase in hardness by both microindentation and instrumented indentation can be attributed to small amount of additional stored work that is present near the top and bottom of the plate. These results corroborate with the tensile test results shown in Figure 3.8 and offer an explanation for the intragranular contrast observed in the BSE images in Figure 2.3.

However, Figure 3.11 shows that the instrumented indentation results are virtually identical between middle and end locations suggesting that the difference in properties observed in the larger size scale compression experiments cannot be captured at this μm sized measurement scale. Instrumented indentation experiments and, to a lesser extent, microhardness measurements are not sensitive to crystallographic orientation effects in BCC metals or are they sensitive to grain size strengthening across the range of grain sizes observed in the rolled + annealed microstructure of the TriLab Ta plate. Compression cylinder experiments are sensitive to orientation hardening, however, further suggesting that the increase in strength observed in the compression cylinder experiments near the end of the plate, shown in Figure 3.5 can be attributed the shift and sharpening of crystallographic texture observed in the EBSD results near the end of the plate, shown in section 3.3.

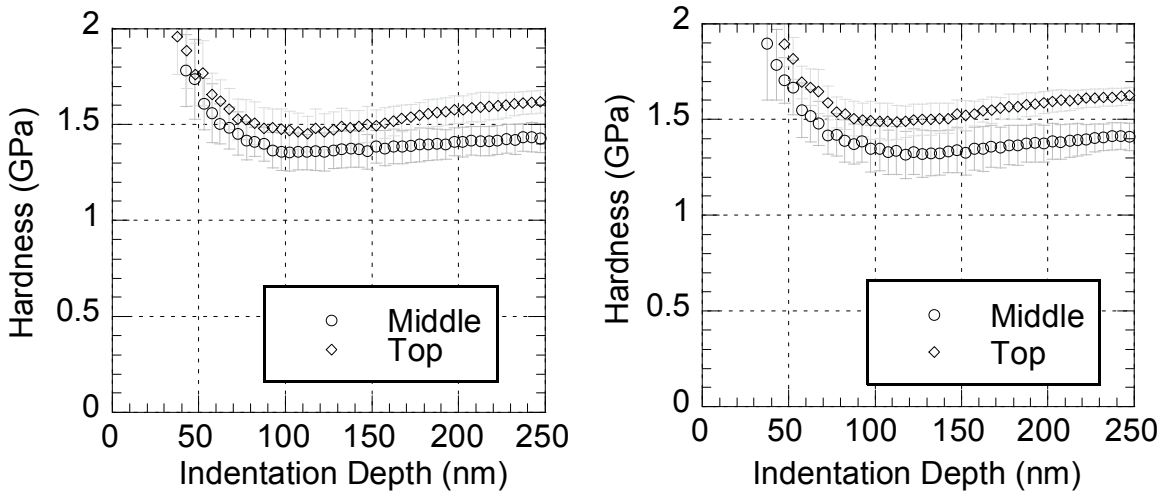

(a) (b)

Figure 3.11 Instrumented indentation results on Ta plate cross-sections, (a) middle and (b) end.

4. SUMMARY AND RECOMMENDATIONS

The TriLab-Ta plate has excellent, uniform, crystallographic texture for a polycrystalline BCC metal. Uniform texture achieved through a highly engineered plate rolling process. The multi-step process includes clock rolling to spread-out the α-fiber texture component ((110) parallel to the rolling direction) and tilt rolling to generate a more uniform distribution of accumulated shear stress in the material during the rolling process to mitigate microstructural banding.

Microstructure characterization revealed evidence of stored work near the top and bottom surface of the plate and an increase in grain size from 25 μm to 39 μm from center to end of the plate (radial position). Subsequent mechanical properties characterization indicated that the affected regions extended inwards approximately 1 inch (25 mm) from the end of the plate and about 2 mm from the top and bottom surfaces. The plate material is otherwise uniform for a wrought and annealed polycrystalline BCC metal.

Convincing evidence of microstructural banding, either by crystallographic texture variation or grain size variation, in the TriLabTa plate's finished condition was not found. Some variation in crystallographic texture was noted by comparing $\langle 001 \rangle / \langle 111 \rangle$ grain orientation ratios relative to the plate normal direction (**ND**). In particular, within the series of higher resolution maps, the ratio inverted from greater than 1 to less than 1 when comparing mapped results from the middle of the plate to mapped results from the top of the plate (TT positions).

Compression cylinder testing revealed a measurable increase in strength, within 25.4mm, from the end of the plate. Tension testing, using the 1/2 sub-size flat specimen geometry, revealed a different stress-strain response near the top of the rolled plate. These results confirmed and further defined the processing 'affected' regions, ~25 mm from the end and ~2 mm from the top and bottom surfaces, where microstructure variations were also noted.

Compression cylinder testing revealed that plate-to-plate variation was not present and did not detect a measurable difference in stress-strain behavior from samples aligned through the thickness of the plate (TT also equivalent to **ND**) when compared with those aligned in the plane of the plate (either IPA or IPB).

Tension and compression test results produced identical yield stresses but different material work hardening response. Several reasons were proposed for this difference.

5. REFERENCES

1. Pedrazas, N.A., Buchheit, T.E., Holm, E.A. and Taleff, E.M.,"Dynamic abnormal grain growth in Tantalum", Materials Science and Engineering A 610, 2014, pp 76-84.

2. Clark, J.B., Garrett, R.K., Jungling, T.L. and Asfahani, R.I., "Influence of Intial Ingot Breakdwon on the Microstructural and Textureal Development of High Purity Tantalum", Metallurgical Transactions A, vol 22A, 1991, 2959-2968.

3. Clark, J.B., Garrett, R.K., Jungling, T.L. and Asfahani, R.I.,"Influence of transverse Rolling on the Micrstructural and Texture Development in Pure Tantalum", Metallurgical Transactions A, vol 23A, 2183-2191.

4. Raabe, D., Schlenkert, G., Weisshaupt, H., and Lucke, K., "Texture and microstructure of rolled and annealed Tantalum", Materials Science and Technology, Vol. 10, 1994, p299-305.

5. Field, D.P., Yanke, J.M., McGowan, E.V. and Michaluk, C.A.,"Microstructurual Development in Asymmetric Processing of Tantalum Plate", Journal of Electronic Materials, Vol. 34, No. 12, 2005, pp. 1521-1525.

6. Refractory metal plates with improved uniformity of texture, 08/05/2008, PCT/US2008/009388

7. Methods and apparatus for controlling texture of plates and sheets by tilt rolling, 08/06/2008, PCT/US2008/009446

8. O. Engler and V. Randle, Introduction to Texture Analysis: Macrotexture, microtexture and Orientation Mapping, Taylor and Francis, 2010, ISBN-10978-1-4200-6365-3.

9. B.D. Cullity and S.R. Stock, Elements of X-Ray Diffraction 3rd Ed., Prentice Hall, 2001 ISBN-10 0201610914

10. Hatherly, M. and Hutchinson, W.B., An Introduction to Texture in Metals, Monograph No. 5, Institution of Metallurgists (Great Britain), 1979, ISBN-0901462055

11. Michaluk, C.A.,"Correlationg Discrete Orientation and grain Size to the Sputter Depositions Properties of Tantalum", Journal of Electronic Materials, Vol. 31, No. 1, 2002, pp. 2-9.

12. Wright, S.I., Gray, G.T. III, and Rollett, A.D.,"Textural and Microstructural Gradient Effects on the Mechanical Behavior of a Tantalum Plate", Metallurgical Transactions A, vol. 25A, 1994, pp. 1025-1031.

13. ASTM E8-13 Standard Test Methods for Tesnion Testing of Metallic Materials, ASTM International, 100 Bar Harbor Drive, PO Box C700, West Conshohocken, PA 19428-2959, 2013.

14. Weinberger, C.R., Battaile, C.C., Buchheit, T.E., and Holm, E.A.,"Incorporating Atomistic data of lattice friction into BCC crystal plasticity models" International Journal of Plasticity, vol. 37, 2012, p.16-30.

15. W.A. Backofen, Deformation Processing, Addison-Wesley Publishing Co, Reading Ma., 1972.

16. Boyce, B.L., Clark, B.G., Lu, Ping, Carroll, J.D., and Weinberger, C.R.,"The morphology of Tensile Failure in Tantalum", Metallurgical and Materials Transactions A, 2013, vol. 44A, pp.4567-4580.

17. Hoge, K.G., and Mukherjee, A.K.,"The temperature and strain rate dependence of the flow stress of tantalum", Journal of Materials Science, vol. 12, 1977, pp. 1666-1672.

18. Chen, S.R. and Gray, G.T., "Constitutive Behavior of Tantalum and Tantalum Alloys", Metallurgical Transactions A, Vol. 27A, 1996, pp. 2994-3006.

19. Khan, A.K. and Liang, R., "Behaviors of three BCC metal over a wide range of strain rates and temperatures: experiments and modeling", International Journal of Plasticity, vol. 15, 1999, 1089-1109.

20. Schwartz, A.J., Lassila, D.H., LeBlanc, M.M.,"The effect of tungsten addition on the microtexture and mechanical behavior of Tantalum plate", Materials Science and Engineering A244, 1998, pp178-190.

21. Kim,J.B. and Shin, H., "Comparison of plasticity models for tantalum anda modification of the PTW model for wide ranges of strain, strain rate, and temperature," Int. J. Impact Eng. 36(5), 746–753 (2009).

22. Barton, N.R. and Rhee, M. "A multiscale strength model for Tantalum over an Extended Range of Strain Rates", Journal of Applied Physics, vol. 114, 123507, 2013.

23. Bronkhorst, C.A., Cerreta, E.K., Xue, Q., Maudlin, P.J., Mason, T.A., and Gray III, G.T.,"An Experimental and Numerical Study of the Localization Behavior of Tantalum and Stainless Steel", International Journal of Plasticity, vol. 22, 2006, pp. 1304-1335.

24. Arsenault, R.J."Effect of Strain Rate and Temperature on Yield Points", Transactions of the Metallurgical Society of AIME", vol. 230, 1964, pp. 1570-1576.

25. Christian J.W.,"Some Surprising Features of the Plastic Deformation of Body-Centered Cubic Metals and Alloys", Metallurgical Transactions A, Vol. 14A, 1983, 1237-1256.

26. Groger, R., Racherla, V., Bassani, J.L., Vitek, V.,"Multiscale modeling of plastic deformation of Molybdenum and Tungsten: II Yield criterion for single crystals based on atomistic studies of glide of ½<111> screw dislocations", Acta Materialia, vol. 56, 2008, pp. 5412-5425.

27. Hull, D., Byron, J.F., and Noble, F.W.,"Orientation Dependence of Yield in Body-Centered Cubic Metals", Canadian Journal of Physics, vol. 45, 1967, 1091-1099.

28. Webb, G.L., Gibala, R., and Mitchell, T.E.,"Effect of Normal Stress on Yield Asymmetry in High Purity Tantalum Crystals", Metallurgical Transactions, Vol. 5, 1974, p1581-1584.

29. ASM Handbook, Vol. 8 Mechanical Testing, Davis, J.R., and Refsnes, S.K., eds., ASM International, 1985, Chp. 8 Hardness Testing.

30. Oliver, W.C. and Pharr, G.M.,"Measurement of hardness and elastic modulus by Instrumented Indentation", J. Mater. Res., Vol. 19(1), p. 3, 2004.

31. ASTM E2546-07 *Standard Practice for Instrumented Indentation Testing*, ASTM International, 100 Bar Harbor Drive, PO Box C700, West Conshohocken, PA 19428-2959, 2007.

32. Bolshakov, A. and Pharr, G.M., "Influences of pileup on the measurement of mechanical properties by load and depth sensing indentation techniques" Journal of Material Research, Vol. 13, No. 4, 1998, 1049-1058.

DISTRIBUTION

5 Lawrence Livermore National Laboratory
Attn: N. Dunipace (1)
P.O. Box 808, MS L-795
Livermore, CA 94551-0808

5 Los Alamos National Laboratory
Attn: Ellen K. Cerreta
P.O. Box 1663
MST-8, Mail Stop G755
Los Alamos, NM 87545

10	MS0889	Thomas Buchheit	1814
1	MS0886	Lisa Deibler	1819
1	MS0886	Joseph Michael	1819
1	MS0889	Jay Carroll	1814
1	MS0889	Brad Boyce	1814
1	MS0889	Corbett Bataille	1814
1	MS1411	Hojun Lim	1814
1	MS1423	Blythe Clark	1111
1	MS0899	Technical Library	9536 (electronic copy)


Sandia National Laboratories